Hybrid Finite Volume Approach to Euler Solutions for Supersonic Flows

M. J. Siclari* and P. Del Guidice†
Grumman Corporate Research Center, Bethpage, New York

A new efficient numerical scheme is presented to solve the Euler equations about three-dimensional surfaces for supersonic flows. The approach utilizes a node-centered, physical space, finite-volume, central-difference scheme with added dissipation that is applied to the crossflow plane terms of the Euler equations. The discretized unsteady Euler equations are then solved by multistage Runge-Kutta integration with local time stepping and residual smoothing to accelerate convergence to a steady state. Three-dimensional flows are treated using an upwind finite-difference scheme for the nonconical terms within the context of a fully implicit marching technique on spherical surfaces. Results for both conical and three-dimensional flows are presented.

Introduction

SOLUTIONS to the Euler equations have been reported by many investigators for both two- and three-dimensional flows. For transonic flows, two- and three-dimensional central-difference Cartesian finite-volume schemes have been reported by Jameson (Refs. 1-3). These schemes utilized multistage, Runge-Kutta, explicit pseudotime integration and added blending of second- and fourth-order dissipation terms for stability and shock capturing. Upwind flux-split implicit schemes have also been developed (see Refs. 4, 6 and 7) and applied to both transonic and supersonic flow problems. Shock fit supersonic conical flow Euler solutions with separated flows have been reported by Marconi (see Refs. 8 and 9). Recently, Powell et al. and Murman et al. (see Refs. 10-12) have developed supersonic conical solutions to the Euler equations for separated flows using a cell-centered central-difference finite-volume scheme with aspects similar to Jameson (Ref. 1) and Rizzi and Eriksson (Ref. 13).

In this report, a numerical scheme is developed, based on Jameson's recent explicit, vortex-based, finite-volume method (see Ref. 3), specifically tailored to supersonic flows about conical and three-dimensional surfaces. The approach is distinct from Murman's for conical flows in that it is composed of a vertex- or node-centered rather than a cell-centered finite-volume scheme. The node-centered scheme eliminates the necessity of extrapolating the pressure terms to the boundary. It also yields more accurate flux estimates on highly skewed or irregular meshes. The added dissipation is very similar to that used by Jameson in Ref. 1.

The three-dimensional unsteady Euler equations are written in a physical space conical/spherical coordinate system. For three-dimensional supersonic flows, the present technique utilizes an upwind marching on spherical surfaces. The upwind treatment of the marching terms has the advantage of not requiring added dissipative terms in the marching direction. Employing spherical surfaces for marching allows the treatment of lower freestream Mach numbers prior to encountering subsonic Mach numbers in the marching direction. This is necessary for the computation of wings in the lower supersonic Mach number regime. The marching is fully implicit in that the nonconical marching terms are included in each stage of the Runge-Kutta integration scheme. Hence, a pseudotime integration is employed to converge to a steady-state solution for each crossflow plane. This essentially eliminates all marching step size stability constraints except those dictated by accuracy requirements.

The three-dimensional implicit marching method treats the crossflow terms in a similar fashion to the conical flow method by using a conical coordinate finite-volume scheme in physical space. The three-dimensional terms are evaluated separately in a computational space in finite-difference form. This, in essence, yields a hybrid method that utilizes the salient features of the unsteady physical space finite-volume method for each crossflow plane with a simple finite-difference upwind treatment for the marching terms.

The present method is shown to produce both attached and separated conical flows. The method is validated against computational and experimental data for both conical flows and an attached three-dimensional supersonic fighter wing (Ref. 14) where full potential solutions with entropy corrections (Ref. 19) are also available for comparison. A three-dimensional body at high angle of attack is also compared to experiment and full potential theory.

Governing Equations

The differential form of the unsteady Euler equations in a Cartesian coordinate system is

$$\frac{\partial Q}{\partial t} + \frac{\partial f}{\partial x} + \frac{\partial g}{\partial y} + \frac{\partial h}{\partial z} = 0 \tag{1}$$

where

$$Q = \begin{bmatrix} \rho \\ \rho u \\ \rho v \\ \rho w \\ e \end{bmatrix}, \quad f = \begin{bmatrix} \rho u \\ P + \rho u^2 \\ \rho uv \\ \rho uw \\ \rho uH \end{bmatrix},$$

$$g = \begin{bmatrix} \rho v \\ \rho uv \\ P + \rho v^2 \\ \rho uw \\ \rho vH \end{bmatrix}, \quad h = \begin{bmatrix} \rho w \\ \rho uw \\ \rho vw \\ P + \rho w^2 \\ \rho wH \end{bmatrix}$$

and ρ, u, v, w, e, P, and H denote nondimensional density, Cartesian velocity components, energy, pressure, and total

Presented as Paper 88-0225 at the AIAA 26th Aerospace Sciences Meeting, Reno, NV, Jan. 11-14, 1988; received Jan. 21, 1988; revision received Feb. 27, 1989.

*Senior Staff Scientist. Associate Fellow AIAA.
†Staff Scientist. Associate Fellow AIAA.

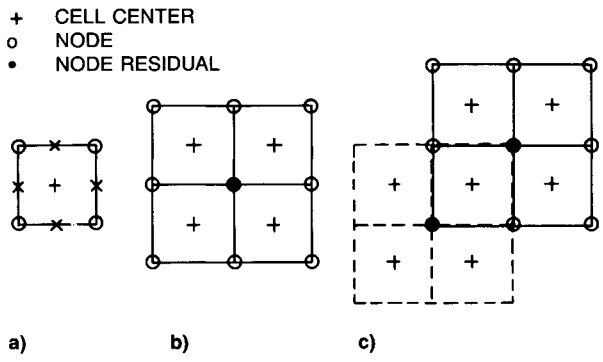

Fig. 1 Schematic of node-centered finite volume scheme: a) individual cell, b) node residual, and c) interlocking residuals.

enthalpy. The pressure and total enthalpy are related to the flow variables by the following expressions:

$$e = \frac{P}{(\gamma - 1)} + \frac{1}{2}\rho\,(u^2 + v^2 + w^2)$$

$$H = \frac{e + P}{\rho} \tag{2}$$

The Cartesian Euler equations can be expressed in a spherical or conical coordinate system by letting

$$\bar{x} = x/z, \quad \bar{y} = y/z, \quad \text{and } R^2 = x^2 + y^2 + z^2$$

The set of partial differential equations (1) transforms to

$$Q_{\hat{t}} + \left(\frac{\partial \bar{f}}{\partial \bar{x}} + \frac{\partial \bar{g}}{\partial \bar{y}} + 2\bar{I}\right) + \frac{R}{\Omega^2}\frac{\partial \bar{h}}{\partial R} = 0 \tag{3}$$

where $\Omega = 1 + \bar{x}^2 + \bar{y}^2$, $\hat{t} = (\Omega/R)t$, and

$$\bar{f} = \begin{bmatrix} \rho\bar{U} \\ \rho u\bar{U} + P \\ \rho v\bar{U} \\ \rho w\bar{U} - \bar{x}P \\ \rho H\bar{U} \end{bmatrix} \quad \bar{g} = \begin{bmatrix} \rho\bar{V} \\ \rho u\bar{V} \\ \rho v\bar{V} + P \\ \rho w\bar{V} - \bar{y}P \\ \rho H\bar{V} \end{bmatrix}$$

$$\bar{h} = \begin{bmatrix} \rho\bar{W} \\ \rho u\bar{W} + \bar{x}P \\ \rho v\bar{W} + \bar{y}P \\ \rho w\bar{W} + P \\ \rho H\bar{W} \end{bmatrix} \quad \bar{I} = \begin{bmatrix} \rho w \\ \rho uw \\ \rho vw \\ \rho w^2 + P \\ \rho Hw \end{bmatrix}$$

and

$$\bar{U} = u - \bar{x}w, \quad \bar{V} = v - \bar{y}w, \quad \text{and} \quad \bar{W} = \bar{x}u + \bar{y}v + w$$

If conical similtude is assumed, the set of partial differential equations (3) reduces to the identical set of equations used in Refs. 10–12 for conical flows on a unit sphere.

Hybrid Finite-Volume Scheme

A hybrid finite-volume approach is used in which a discretized integral formulation is applied to the crossflow terms in Eq. (3) and a simple finite-difference approximation is developed for the R derivatives in the marching direction. Equation (3) can be expressed in integral form as

$$\frac{\partial}{\partial_{\hat{t}}}\int\int_S Q\,d\bar{x}\,d\bar{y} + \int(\bar{f}\,d\bar{y} - \bar{g}\,d\bar{x}) + 2\int\int_S \bar{I}\,d\bar{x}\,d\bar{y} + \frac{R}{\Omega^2}\int\int_S \frac{\partial h}{\partial R}\,d\bar{x}\,d\bar{y} = 0 \tag{4}$$

Crossflow Plane Scheme

A node-centered conical coordinate finite-volume scheme following Jameson's approach is applied to a discretized version of Eq. (4) in the crossflow plane. Figure 1 illustrates the basic scheme. It is assumed that the residual and, hence, the flow variables are stored at node points. The cell-centered fluxes are first computed over each cell of the grid by summing the fluxes across the four individual sides of the cell. Since flow variables are stored at node points, the side flux is computed by simply averaging the fluxes stored at the endpoints or nodes of each side constituting the boundaries of a cell. This yields a more accurate estimate for the flux on skewed or irregular meshes in comparison to a cell-centered scheme. The residual at each node point is then computed by summing the cell-centered fluxes of the four cells surrounding that node point. In discretized form, the conical terms in Eq. (4) can be rewritten at a node point i, j as

$$\Delta S\frac{\Delta Q}{\Delta\hat{t}} + \sum_{\text{cell}=1}^{4}\sum_{\text{side}=1}^{4}(\bar{f}\Delta\bar{y} - \bar{g}\Delta\bar{x}) + 2\bar{I}\Delta S = 0 \tag{5}$$

where $\bar{f}$ and $\bar{g}$ are the side fluxes and

$$\Delta S = \sum_{\text{cell}=1}^{4}\Delta A$$

The area ΔS is the sum of the area of the four cells surrounding a node point. Hence, the formulation of the node residuals is composed of an interlaced pattern of four cells.

Dissipation and Local Time Stepping

A blend of second- and fourth-order differences adopted from Jameson (Ref. 1), but similar to Rizzi et al. (Ref. 13) and Murman et al. (Ref. 12), is used for added artificial dissipation. The fourth-order differences are added as background dissipation to prevent odd and even point decoupling. The second-order differences are added primarily to smooth out oscillations in regions of severe pressure gradients associated with shock capturing. The second- and fourth-order dissipation has the following function forms:

$$D_2Q = \epsilon_2\left[\delta_{\bar{x}}\left(\frac{\Delta S}{\Delta t^*}\bar{P}_{\bar{x}\bar{x}}\delta_{\bar{x}}Q\right) + \delta_{\bar{y}}\left(\frac{\Delta S}{\Delta t^*}\bar{P}_{\bar{y}\bar{y}}\delta_{\bar{y}}Q\right)\right]$$

$$D_4Q = \epsilon_4\left[\delta_{\bar{x}}\left(\frac{\Delta S}{\Delta t^*}\delta_{\bar{x}}{}^3Q\right) + \delta_{\bar{y}}\left(\frac{\Delta S}{\Delta t^*}\delta_{\bar{y}}{}^3Q\right)\right] \tag{6}$$

where ϵ_2 and ϵ_4 are dissipation constants, a proper order of magnitude is obtained through the scaling $\Delta S/\Delta t^*$ next defined, and $P_{\bar{x}\bar{x}}$, $P_{\bar{y}\bar{y}}$ are pressure switches.

The coefficients of the dissipative terms are scaled by the total cell area or sum of the four cell areas surrounding a node. Local time stepping is used to accelerate convergence. Δt^* denotes the local time step at a node for a fixed CFL number of unity. The local time step is evaluated for each cell, and the nodal time step is taken to be the average of the four

surrounding cell time steps. The local time step for a cell is evaluated as

$$\Delta t^* = \frac{\Delta A}{\Delta \ell_i (a + |Q_N|)_i + \Delta \ell_j (a + |Q_N|)_j} \tag{7}$$

where a is the speed of speed, $\Delta \ell$ the side length, and Q_N the normal velocity through the side.

The denominator in Eq. (7) is taken to be the average of $(a + |Q_N|)$ divided by the average side length in the two coordinate directions. Hence, the dissipation coefficient $\Delta S/\Delta t^*$ becomes the order of the average grid size and proportional to the largest wave speed $(a + |Q_N|)$. In the time stepping scheme, a locally varying time step $\Delta t = \lambda \Delta t^*$ is used, where the actual CFL number λ may also be varied. Since the dissipation is scaled according to Δt^*, the steady-state solution is independent of the actual choice of CFL number.

Boundary Conditions

On the body, the normal velocity is set equal to zero at node points. Since the governing equations are satisfied at node points rather than cell centers, there is no necessity to extrapolate pressure to the boundary. At the outer boundary, which is taken beyond the captured bow shock, two outer rings are set to freestream conditions.

Nonconical Upwind Scheme

To evaluate the R derivatives for nonconical flows, an arbitrary transformation from the physical conical coordinates $(\bar{x}, \bar{y}, R)$ to a computational grid (ξ, η, ζ) is assumed where

$$\xi = (\bar{x}, \bar{y}, R), \quad \eta = (\bar{x}, \bar{y}, R), \quad \zeta = R \tag{8}$$

The nonconical term in the differential equation (3) is transformed into

$$\frac{\partial \bar{h}}{\partial R} = \xi_R \bar{h}_\xi + \eta_R \bar{h}_\eta + \bar{h}_\zeta \tag{9}$$

where derivatives with respect to the marching direction ζ (i.e., R) are upwinded by a first-order backward difference.

Multistage Integration Scheme

The unsteady governing equation can then be represented as

$$\frac{\partial Q}{\partial t} + \frac{1}{\Delta S} R_{\bar{x}\bar{y}}(Q) + \frac{1}{\Delta S} D_{\bar{x}\bar{y}}(Q) + H_R(Q) = 0 \tag{10}$$

where the operator $R_{\bar{x}\bar{y}}$ represents the crossflow finite-volume spatial approximation to the residual, $D_{\bar{x}\bar{y}}$ the added second- and fourth-order dissipative operator, and H_R the nonconical upwind operator. A modified fourth-order Runge-Kutta scheme is used to integrate the set of ordinary differential equations defined by Eq. (10) in the following form:

$$Q_{ijk}^{(0)} = Q_{ijk}^{(n)}$$

$$Q_{ijk}^{(\ell)} = Q_{ijk}^{(0)} - \alpha_\ell \frac{\Delta t}{\Delta S} \left[\left(R_{xy}^{(\ell)} + D_{xy}^{(0)} \right) + \frac{\Delta S}{\Delta R} \left(H_{ijk}^{(0)} - H_{ijk} \right) \right]$$

$$Q_{ijk}^{(n+1)} = Q_{ijk}^{(4)} \tag{11}$$

where $\alpha = 1/4, 1/3, 1/2, 1$, i and j indices refer to the crossflow plane coordinates $\bar{x}$ and $\bar{y}$, respectively, and the k index refers to the marching plane. The bracketed superscripts refer to the ℓ stages (i.e., $\ell = 4$) of the Runge-Kutta scheme. The dissipative terms are frozen throughout the multistage integration scheme. The nonconical or three-dimensional terms are evaluated upwind from the current k plane to the previous $k - 1$ plane. Hence, the previous plane information is frozen throughout the time integration scheme, and the current plane nonconical contribution to the residual is updated implicitly for each stage of the multistage scheme.

The implicit treatment of the nonconical terms removes any CFL constraints in the marching direction. The method begins at $R = \Delta R$ where a small conical nose cap at the apex is assumed. As a result, both planes of information at $R = 0$ and $R = \Delta R$ are set equal, resulting in the automatic reduction of the equations to conical flow. Marching then begins using the conical solution at $R = \Delta R$ as initial conditions for the subsequent three-dimensional solution. All subsequent marching planes use the solutions from the previous plane as an initial guess.

Residual Smoothing

In order to accelerate convergence, an implicit residual smoothing (Ref. 2) is applied to the current plane in the following fashion:

$$(1 - \mu_{\bar{x}} \delta_{\bar{x}}^2)(1 - \mu_{\bar{y}} \delta_{\bar{y}}^2) \bar{R}_{i,j} = R_{i,j} \tag{12}$$

where $\bar{R}_{i,j}$ is the smoothed residual. The residual smoothing requires two tridiagonal inversions and is quite costly computationally. For efficiency, it was found adequate to use residual smoothing only on the second and last stage of the Runge-Kutta integration scheme. The constants $\mu_{\bar{x}}$ and $\mu_{\bar{y}}$ may have typical values ranging from 0.25 to unity.

Discussion of Conical Flow Results

Convergence to a Steady State

Figure 2 shows plots of the maximum residual vs both CPU time and iterations on the Cray XMP for a sample conical flow case. The example case is an elliptic cone (20 deg by 1.5 deg) at $M_\infty = 2.0$, $\alpha = 10$ deg. The grid is a 61×51 mesh that is generated by a conformal mapping that clusters points around the leading edge. Additional clustering was used in the radial direction to cluster points in the vicinity of the surface. Figure 3a shows the overall grid and Fig. 3b illustrates the overall isobar solution obtained for this mesh. All shocks are captured. As a result, the radial clustering varies circumferentially in order to accurately capture the windward bow shock.

All the convergence histories shown in Fig. 2 are for an impulsive start from freestream conditions using a locally varying Δt with a constant CFL number. The solid line represents a nominal case in which the residual smoothing is turned off. The dashed and broken lines show the convergence histories with the residual smoothing turned on only at the two even stages (i.e., the second and fourth) of the Runge-Kutta scheme. Significant gains are achieved initially with a smoothing coefficient of 0.25 in both directions. A further increase in the smoothing coefficient shows only modest gains, and a smoothing coefficient of 0.50 appears to be optimum. Additional increases in the smoothing coefficient show no meaningful gains and can cause the convergence rate to deteriorate. The effectiveness of the residual smoothing is both case- and grid-dependent. Much greater improvements in convergence rates have been achieved for simpler flow situations and less severely clustered grids. With the residual smoothing turned on, the solution converged to machine zero in about 45 CPUs. For all practical purposes, the solution was converged (i.e., six to eight orders of magnitude) in about 15 to 20 s. The CPU efficiency reflects the highly vectorizable nature of the explicit Runge-Kutta scheme. Even the residual smoothing was vectorized for the most part.

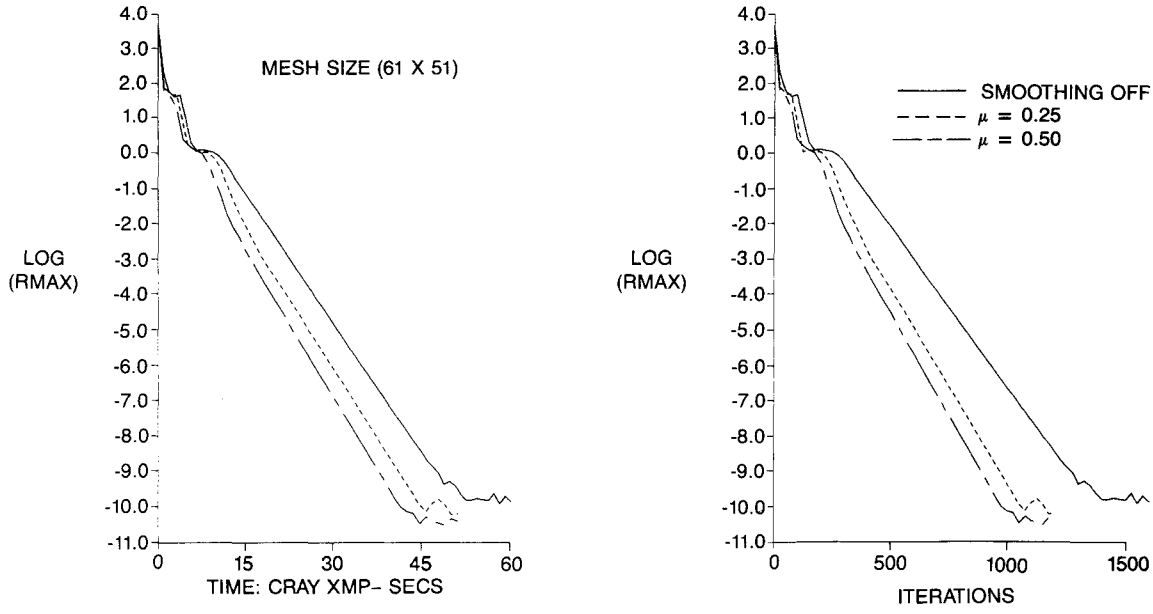

Fig. 2 Effects of residual smoothing on the convergence of an elliptic cone, $M_\infty = 2.0$, $\alpha = 10$ deg.

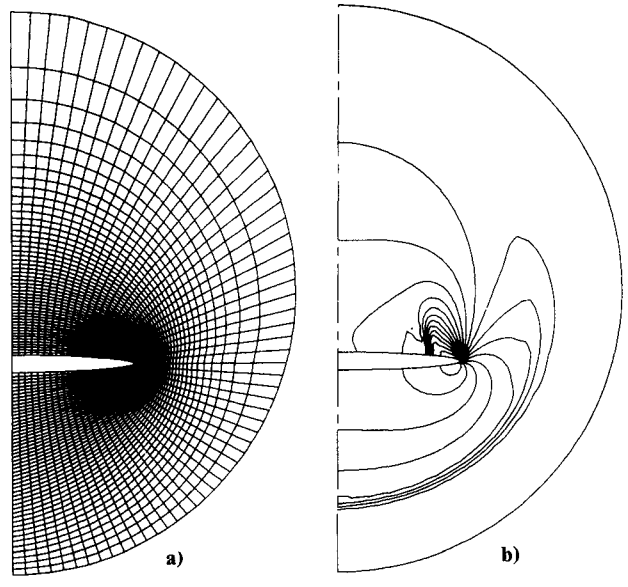

Fig. 3 Grid and isobar solution for an elliptic cone at $M_\infty = 2.0$, $\alpha = 10$ deg. a) Computational grid (61 × 51) and b) isobar pattern.

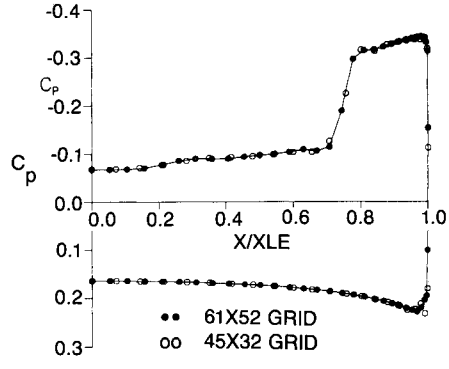

Fig. 4 Surface pressure distribution on an elliptic cone at $M_\infty = 2.0$, $\alpha = 10$ deg.

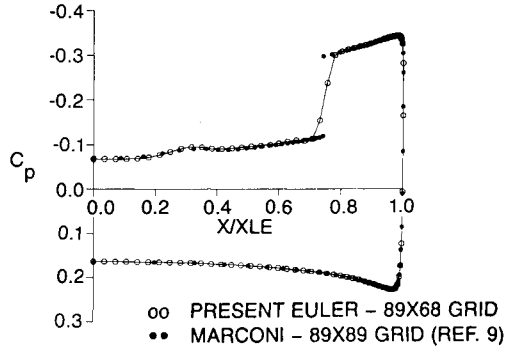

Fig. 5 Comparison of surface pressures for an elliptic cone at $M_\infty = 2.0$, $\alpha = 10$ deg.

Artificial Dissipation

Figure 4 shows the surface pressure coefficient distribution obtained on the 61 × 51 grid and also on a coarser grid of 45 × 32 for the conical flow on the elliptic cone just discussed. Both of these coarse grid solutions represent attached leading-edge flows with a small shock vorticity-induced separation inboard of the crossflow shock. These solutions were generated using minimum values of the dissipation coefficients. Hence, the correct inviscid solution for this case can be obtained with very crude grids. Earlier studies using central-difference methods (see Ref. 5) had indicated that very fine grids were necessary to compute the attached leading-edge solution for this case. The present method is in agreement with later studies such as Ref. 20 or Ref. 21 that also demonstrated attached leading-edge solutions on crude grids.

Figure 5 shows how the present method compares with the shock fit method of Marconi (Ref. 9). The present method used a mesh of 89 × 68. The method of Ref. 9 used an 89 × 89 grid and additional clustering around the ellipse that put more points in the vicinity of the leading edge and inboard shock foot location. Both bow and crossflow shocks are fit (in Ref. 9), whereas the present method captures both these shocks. Given the differences in grid, both methods show quite good agreement for surface pressures and crossflow shock locations.

Attached Flows

Figure 6 shows a set of surface pressure coefficient solutions for a conically cambered wing at $M_\infty = 1.6$ and $M_\infty = 2.0$.

Experimental data were available, and the Euler solutions were computed for the highest angle of attack obtained in the wind-tunnel data (Ref. 16). Nonconservative full potential flow solutions also were generated using the relaxation method of Ref. 19. The Euler solutions captured both bow and embedded shocks using an 89×65 stretched and mapped grid. The full potential solutions were obtained on similar grids (73×57) with the bow shock fit. Excellent, if not remarkable, agreement is obtained between the Euler and full potential solutions. Both agree reasonably well with the test data. Some discrepancies exist with the experiments near the leading edge where the computed solutions show a lower suction peak. Differences in crossflow shock location are evident at the higher Mach number possibly due to boundary-layer shock interaction effects. The experimental data show little or no separation.

Separated Flows

Figure 7 shows a set of surface pressure coefficient solutions for a conical wing at $M_\infty = 1.70$ and 2.80. The upper surface is flat with a sharp leading edge. The mapped grid was generated by locating a grid point at the leading edge. Other than this, no special considerations were used in generating the Euler solutions on an 89×65 grid. Upper-surface experimental data (Ref. 17) were available, but needed corrections to the angle of attack due to sting effects and an angle rotation due to differences in coordinate origins. The corrected angle of attack computed for both cases was approximately 14 deg and is shown in Fig. 7.

Figure 8 shows the leading-edge separation streamlines and supersonic crossflow Mach number regions, denoted by the dashed lines, for both of the aforementioned comparisons. In both cases, the flow separates at the leading edge and forms a

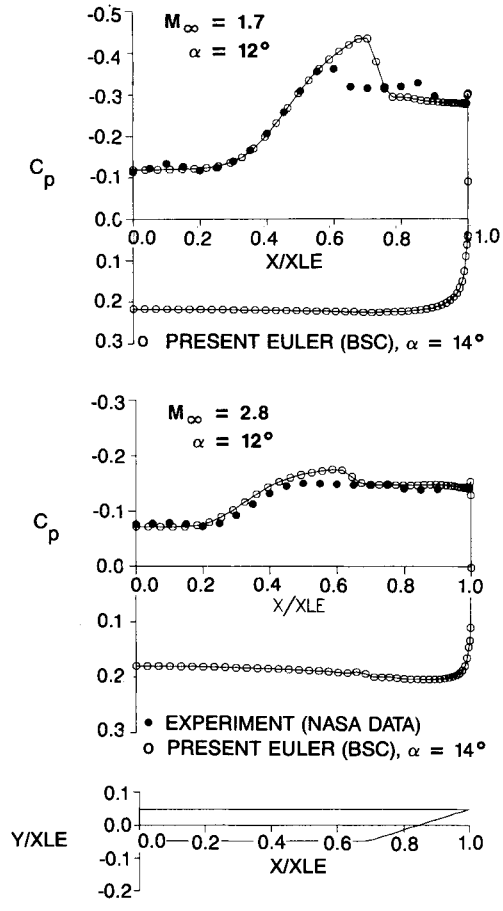

Fig. 7 Surface pressure comparisons for a conical vortex flap wing at $M_\infty = 1.7$ and 2.8.

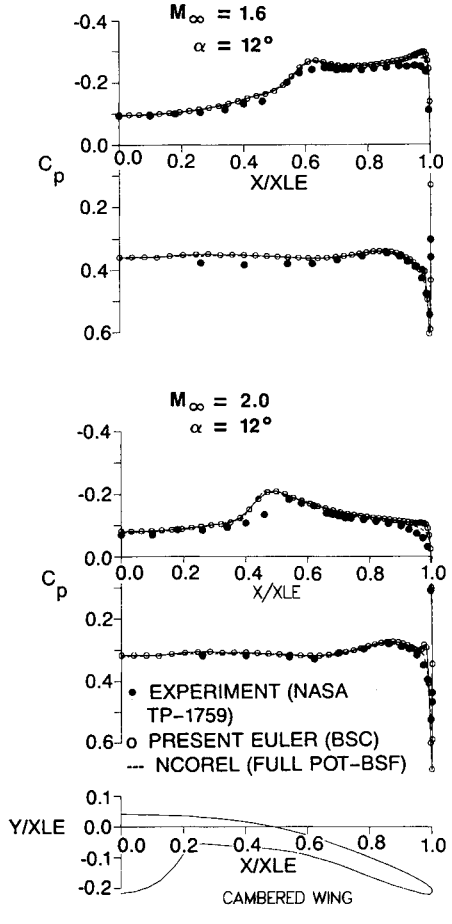

Fig. 6 Surface pressure comparisons for a conically cambered wing at $M_\infty = 1.6$ and 2.0.

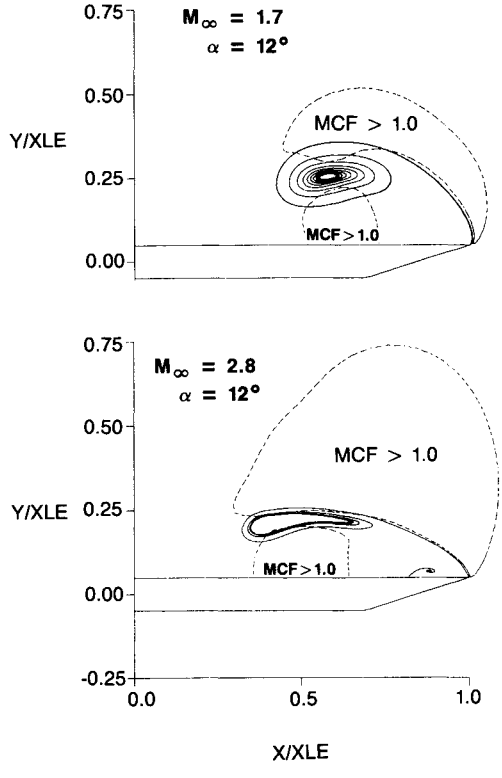

Fig. 8 Leading-edge separation streamlines and crossflow sonic lines at $M_\infty = 1.7$ and 2.8.

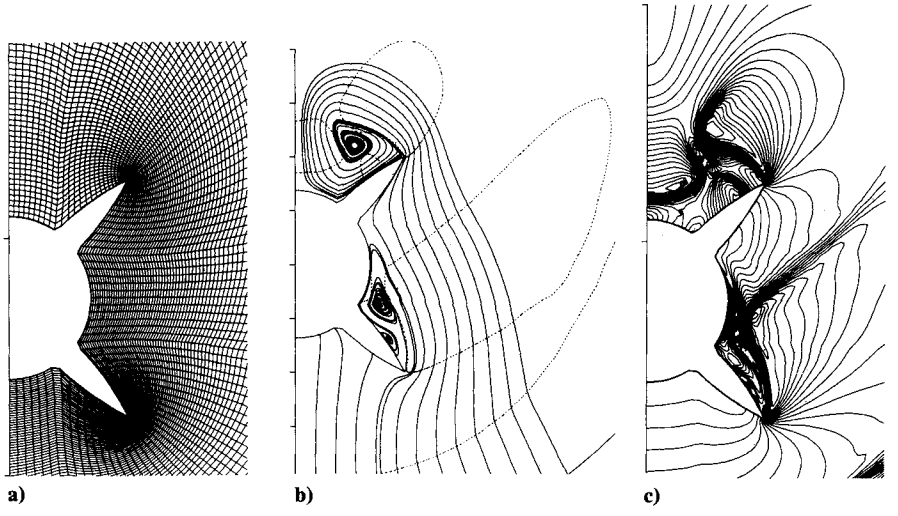

Fig. 9 Computed results for a conical mutlifinned cross section at $M_\infty = 2.0$, $\alpha = 35$ deg. a) Mesh (95 × 72), b) crossflow streamlines, and c) crossflow isomach contours.

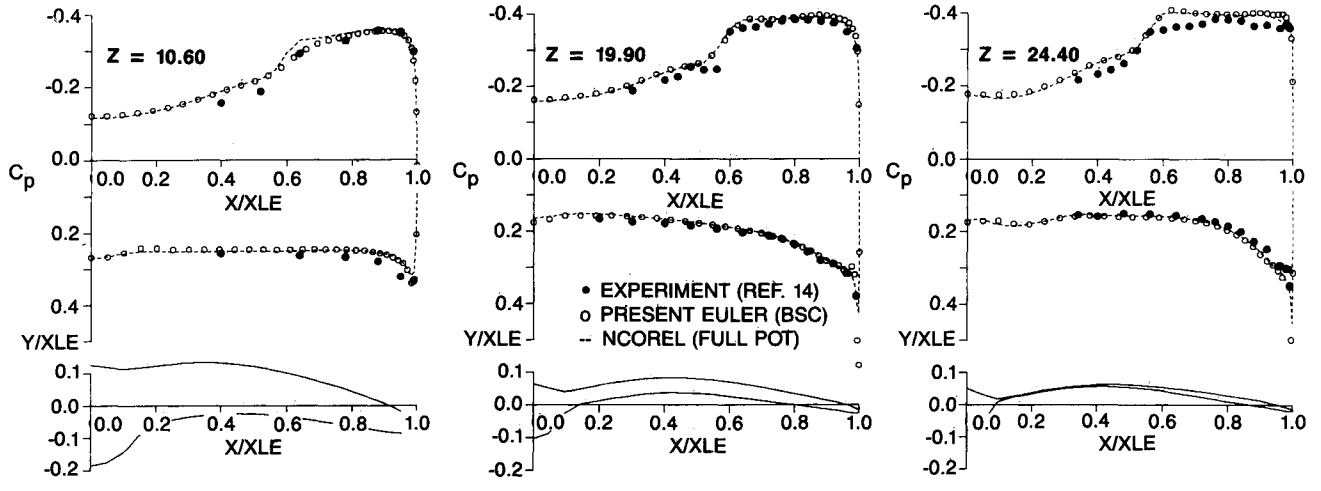

Fig. 10 Surface pressure comparisons for a three-dimensional supersonic wing at $M_\infty = 1.6$, $\alpha = 14$ deg.

spiraling streamline or vortex. Two supersonic crossflow regions are present for both freestream Mach numbers, indicating reverse crossflow shocks. The flow under the spiral accelerates toward the leading edge, forming another supersonic reverse crossflow region terminating in a crossflow shock. This is also indicated in the computed Euler pressure distributions shown in Fig. 7. At the higher Mach number of 2.8, the reverse crossflow shock is strong enough to induce a small secondary spiral. The Euler solutions are in good agreement with the experiment up to the reverse crossflow shock. Evidently, viscous effects dominate the flow via boundary-layer shock-induced separation.

Figure 9 shows a series of computed results for a multifinned conical cross section at $M_\infty = 2.0$, $\alpha = 35$ deg. Fig. 9a shows a portion of the grid used for the computation. The fins have sharp leading edges and are located symmetrically at ±45 deg. The fins are swept 70 deg and are attached to a 10 deg conical centerbody. The grid was generated with a series of analytic conformal mappings. The mapped space was then partitioned into three regions to yield the grid shown in Fig. 9a. Figure 9b shows some of the computed crossflow streamlines and crossflow sonic lines, and Fig. 9c shows the crossflow Mach contours. A very complex flow pattern exists for this conical cross section. Both fins separate and vortices are formed. Two supersonic crossflow regions exist near the lower fin and three in the vicinity of the upper fin. The supersonic crossflow Mach number region near the lower fin is quite large, extending almost to the bow shock. A very strong crossflow shock occurs on top of the lower fin vortex. A "pinwheel" shock or triad of shocks occurs around the upper fin vortex. On the lower fin, a secondary reverse flow vortex also develops, induced by the vorticity of the reverse crossflow shock. At this freestream condition, slightly subsonic total Mach numbers exist on the windward surface. Such a complex flow pattern as indicated by these results probably should warrant finer grids to reveal additional details of the flow pattern.

Discussion of Three-Dimensional Flow Results

For three-dimensional flows, the computation is initiated by assuming a small conical nose cap for the three-dimensional geometry. Arbitrary step sizes can be used for marching over the configuration. Typically 30 to 100 marching steps are used. At each marching step, the unsteady equations are solved with an implicit update of the R derivatives. For a three-dimensional configuration, typically the solution is converged to 10^{-3} at each crossflow plane, representing a 4 to 7 order-of-magnitude drop in maximum residual. Each nonconical cross section typically requires 50 to 300 iterations to

converge, but this number is largely dependent on marching step size, geometry, grid, and severity of the case.

Three-Dimensional Wing: Attached Flow

Euler solutions were computed for a three-dimensional supersonic fighter wing. Experimental data are available for this wing at four spanwise data stations. The Euler code was run up to the highest angle of attack available in the data at $M_\infty = 1.6$, $\alpha = 14$ deg. The full potential solution was also computed. It utilizes a fully implicit spherical marching method similar to the Euler code. Hence, almost identical grids were used for both computations. The Euler code used a 65×57 crossflow grid with all shocks captured, and the full potential code used a 65×57 grid with the bow shock fit. Both computations were carried out using only 30 marching planes with a radial step size of unity. Figure 10 shows a comparison of surface pressures for Euler, full potential, and test data at three spanwise stations for $M_\infty = 1.6$ and $\alpha = 14$ deg. Once again, excellent, if not remarkable, agreement is shown between the Euler and full potential solutions at all spanwise stations. Slightly different computed crossflow shock locations are exhibited at the first station. At the first station, the Euler solution shows slightly better agreement with the test data in the vicinity of the crossflow shock. Both the Euler and full potential computations are in good agreement with the test data. The experimental data show little or no separation. The largest discrepancy occurs inboard of the crossflow shock. Figure 11 shows isobar patterns for the wing at $M_\infty = 1.6$ and $\alpha = 12$ and 14 deg. The crossflow shock is quite evident on the leeside of the wing at $\alpha = 14$ deg.

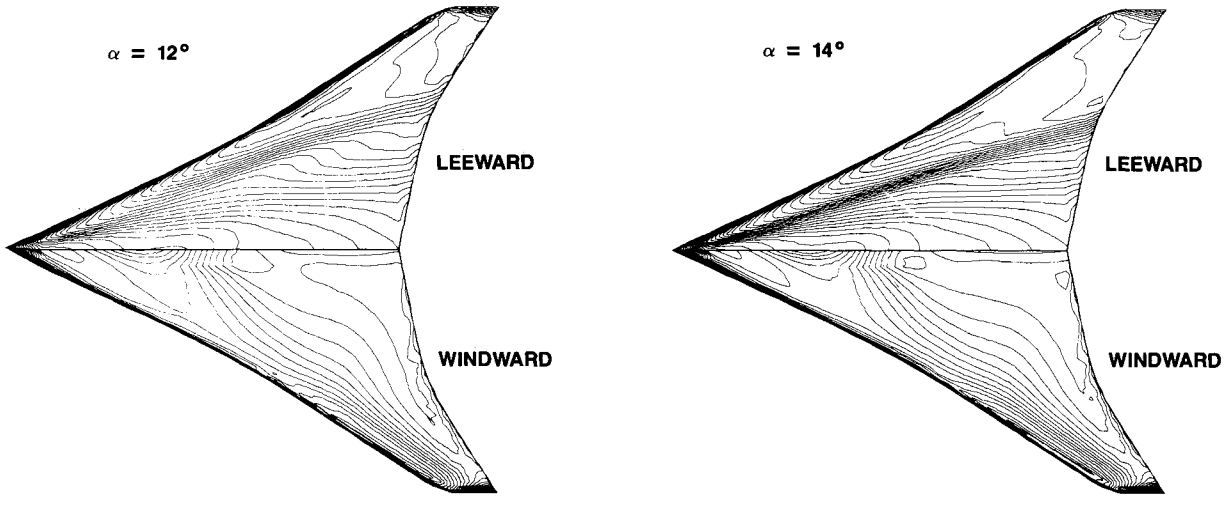

Fig. 11 Surface pressure contours for a three-dimensional supersonic wing at $M_\infty = 1.6$.

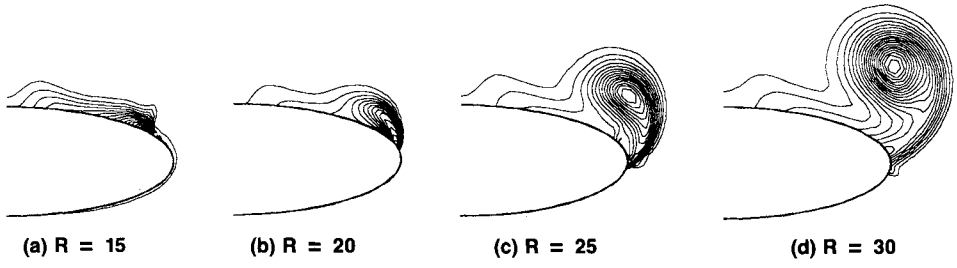

Fig. 12 Entropy contours for a three-dimensional body at $M_\infty = 2.50$, $\alpha = 10$ deg.

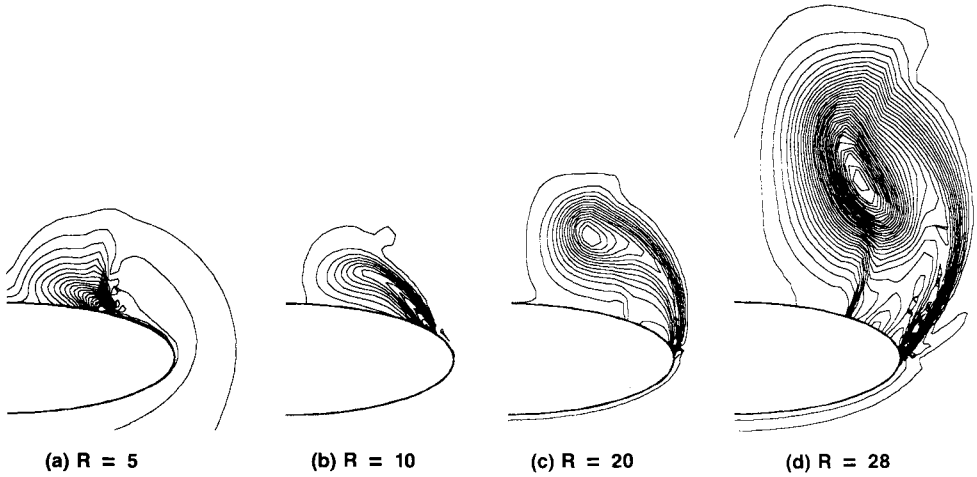

Fig. 13 Entropy contours for a three-dimensional elliptical body at $M_\infty = 2.50$, $\alpha = 20$ deg.

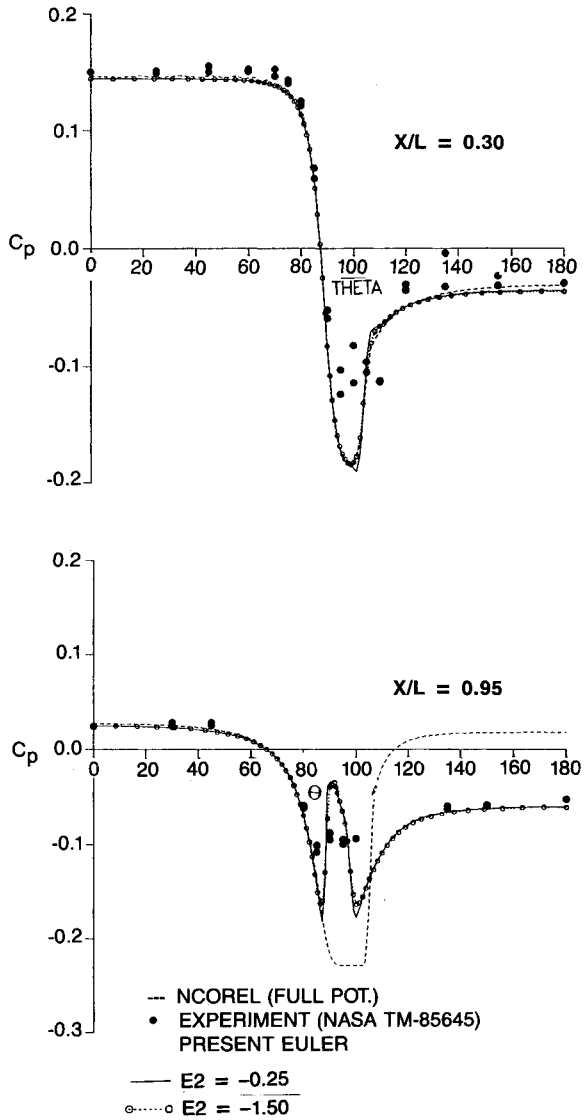

Fig. 14 Surface pressure comparisons for a three-dimensional elliptical body at $M_\infty = 2.5$, $\alpha = 10$ deg.

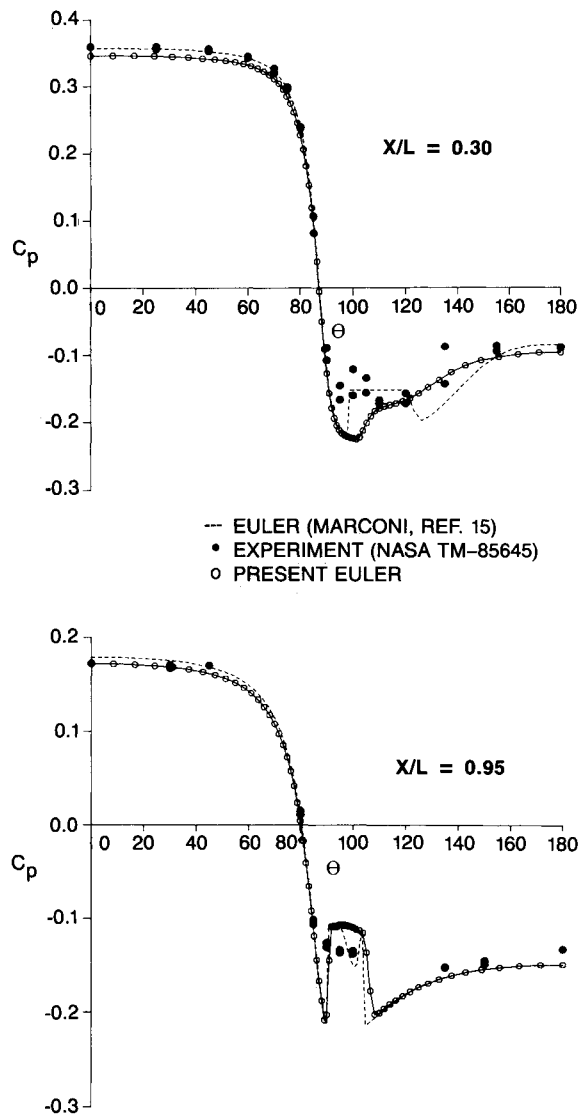

Fig. 15 Surface pressure comparisons for a three-dimensional body at $M_\infty = 2.50$, $\alpha = 20$ deg.

Three-Dimensional Body-Separated Flows

The Euler solutions shown for the wing agree remarkably well with the full potential solution. This is because the wing has primarily attached flow due to a rounded leading edge and camber designed to minimize the generation of crossflow shock waves. For separated flows, detailed experimental data (Ref. 18) are available for a three-dimensional body with a 3:1 elliptic cross section and a modified Haacke-Adams area distribution. The Euler solutions for this problem were generated at $M_\infty = 2.50$ and $\alpha = 10$ and 20 deg, and used only 30 marching planes with a 65 × 57 crossflow plane grid. The evolution of the flowfield at $\alpha = 10$ deg is depicted by the total pressure or entropy contours shown in Fig. 12 at several crossflow stations with $R = 30$ corresponding to the last computed station. Up to $R = 15$, a crossflow shock is situated on the leeside of the section. As the body expands, the crossflow shock migrates toward the leading edge. As the crossflow shock migrates toward the leading edge, it grows in strength, and separation is increasingly induced downstream of this shock. At $R = 25$, the crossflow shock is located close to the shoulder and a distinct vortex has developed.

Figure 13 shows the evolution of the flowfield in terms of entropy or total pressure contours at $M_\infty = 2.5$, $\alpha = 20$ deg. At this higher angle of attack, crossflow shock vorticity-induced separation occurs earlier as indicated at $R = 5$. It should be noted that at this station the flow around the leading edge is attached. Again as the body expands, the crossflow shock becomes stronger and migrates toward the leading edge. At $R = 20$, a large vortex has developed with a reverse crossflow shock underneath. From $R = 20$ to $R = 30$, the vortex increases dramatically in size.

Figure 14 compares the Euler, full potential, and experimental surface pressure coefficients at two span stations for $M_\infty = 2.50$ and $\alpha = 10$ deg. The Euler and full potential solution are in excellent agreement at $X/L = 0.30$, and both indicate a crossflow shock on the leeside of the body. Aside from the leeside suction region, both solutions are in good agreement with the experimental data. The experimental data indicate separation dominated by viscous effects in the suction region. At $X/L = 0.95$. the Euler solution predicts shock-induced separation due to the strong shock vorticity. The irrotational assumption of the full potential equation does not permit shock vorticity-induced separation that will occur for the Euler equations as the shock strength increases. The full potential solution predicts a suction pressure plateau near vacuum pressure, terminating in a very strong crossflow

shock. The Euler solution does not expand to vacuum pressure but indicates a crossflow shock slightly upstream of the shoulder at $\theta = 85$ deg. The Euler solution also predicts a reverse crossflow shock at $\theta = 95$ deg. The experimental data do not indicate either of these shocks and do not achieve the suction levels that the Euler solution predicts. Away from the shoulder region, however, the Euler solution is in excellent agreement with the experiment. Two Euler solutions are shown in Fig. 14 where the second-order dissipation coefficient ($E2$) was increased by a factor of 6. The Euler solutions show only a small effect due to dissipation.

Figure 15 shows a similar comparison at $\alpha = 20$ deg. The full potential solution could not be computed for this case, but the present Euler solution is compared to another Euler solution computed by Marconi in Ref. 15. The Euler solution of Ref. 15 was computed using a completely different finite-difference method and forced separation at the shoulder. Shock vorticity-induced separation is indicated by the present Euler solution at $X/L = 0.30$. The Euler solution of Ref. 15 indicates a crossflow shock just downstream of the shoulder, a constant suction plateau, and a reverse crossflow shock. At $X/L = 0.95$, the two Euler solutions are in excellent agreement. Both predict crossflow and reverse crossflow shocks. One difference between the two Euler results is that the solution of Ref. 15 indicates a reverse crossflow shock separation, whereas the present solution does not. Once again, both Euler solutions are in good agreement with the test data except in the vicinity of the leeside shoulder.

Conclusions

For supersonic three-dimensional flows, a new Euler method has been developed that is both computationally and storage-efficient. Pseudotime integration with residual smoothing is utilized to accelerate crossflow plane convergence to a steady-state solution. The method has been demonstrated to be extremely flexible in predicting a variety of both attached and separated conical and three-dimensional flows. It has been demonstrated that the method is ideally suited for the computations of flows in the lower supersonic Mach regime due to its implicit nature. Accurate three-dimensional solutions can be obtained utilizing as few as 30 marching planes.

Acknowledgment

The authors would like to thank Dr. Antony Jameson of Princeton University for his helpful guidance and suggestions during the course of this work.

References

[1]Jameson, A. and Schmidt, W., "Numerical Solutions of the Euler Equations by Finite Volume Methods Using Runge-Kutta Time-Stepping Schemes," AIAA Paper 81-1259, June 1981.

[2]Jameson, A., "Transonic Flow Calculations for Aircraft," Lecture Notes in Mathematics, Vol. 1127, *Numerical Methods in Fluid Dynamics,* Springer-Verlag, New York, 1985, pp. 156–242.

[3]Jameson, A. "A Vertex Based Multigrid Algorithm for Three-dimensional Compressible Flow Calculations," presented at the ASME Symposium on Numerical Methods for Compressible Flow, Anaheim, CA, Dec. 1986.

[4]Anderson, W. K. and Thomas, J.L., "A Comparison of Finite Volume Flux Vector Splittings for the Euler Equations," AIAA Paper 85-0122, Jan. 1985.

[5]Newsome, R.W., "A Comparison of Euler and Navier-Stokes Solutions for Supersonic Flow over a Conical Delta Wing," AIAA Paper 85-0111, Jan. 1985.

[6]Thomas, J. L., van Leer, B., and Walters, R.W., "Implicit Flux-Split Schemes for the Euler Equations," AIAA Paper 85-1680, July 1985.

[7]Newsome, R.W. and Thomas, J. L., "Computation of Leading Edge Vortex Flows," Vortex Flow Aerodynamics Conference, NASA Langley Res. Ctr. Hampton, VA, Oct. 8–10, 1985.

[8]Marconi, F., "Supersonic Conical Separation due to Shock Vorticity," *AIAA Journal*, Vol. 22, Aug. 1984, pp. 1048–1055.

[9]Marconi, F., "Shock Induced Vortices on Elliptic Cones in Supersonic Flow," AIAA Paper 85-0433, Jan. 1985.

[10]Powell, K., Murman, E., Perez, E., and Baron, J., "Total Pressure Loss in Vortical Solutions of the Conical Euler Equations," AIAA Paper 85-1701, July 1985.

[11]Murman, E.M., Rizzi, A., and Powell, K., "High Resolution Solutions of the Euler Equations for Vortex Flows," *Progress & Supercomputing in Computational Fluid Dynamics,* Birkhauser-Boston, Inc., 1985.

[12]Murman, E.M. and Powell, K., "Comparison of Computations and Experimental Data for Leading Edge Vortices— Effects of Yaw and Vortex Flaps," AIAA Paper 86-0439, Jan. 1986.

[13]Rizzi, A. and Eriksson, L.E., "Computation of Flow Around Wings Based on the Euler Equations," *Journal of Fluid Mechanics*, Oct. 1984.

[14]Mason, W. H., Siclari, M.J., Miller, D.S., and Pittman, J.L., "A Supersonic Maneuver Wing Designed for Nonlinear Attached Flow," AIAA Paper 83-0415, Jan. 1983.

[15]Marconi, F., "Fully Three-Dimensional Separated Flows Computed with the Euler Equations," AIAA Paper 87-0451, Jan. 1987.

[16]Miller, D. S., Landrum, E. J., Townsend, J. C., and Mason, W. H., "Pressure and Force Data for a Flat Wing and a Warped Conical Wing Having a Shockless Recompression at Mach 1.62," NASA TP-1759, April 1981.

[17]Miller, D. S. and Wood, R. M., "Lee-Side Flow over Delta Wings at Supersonic Speeds," NASA TP-2430, June 1985.

[18]Allen, J. M., Hernandez, G., and Lamb, M., "Body-Surface Pressure Data on Two Monoplane-Wing Missile Configurations with Elliptical Cross Sections at Mach 2.50," NASA TM-85645, Sept. 1983.

[19]Siclari, M. J., "The NCOREL Computer Program for 3D Nonlinear Supersonic Potential Flow Computations," NASA CR3694, Aug. 1983.

[20]Kandil, O. A., Chung, A.N., and Shifflette, J.M., "Finite-Volume Euler and Navier-Stokes Solvers for Three-Dimensional and Conical Vortex Flows over Delta Wings," AIAA Paper 87-0041, Jan. 1987.

[21]Kandil, O. A. and Chung, A., "Influence of Numerical Dissipation in Computing Supersonic Vortex-Dominated Flows," AIAA Paper 86-1073, May 1986.